# Space-Confined Synthesis of Monolayer Graphdiyne in MXene Interlayer

*Jiaqiang Li,* Haicheng Cao, Qingxiao Wang, Hui Zhang, Qing Liu, Cailing Chen, Zhan Shi, Guanxing Li, Ya Kong, Yichen Cai, Jie Shen, Ying Wu, Zhiping Lai,* Yu Han, and Jin Zhang**

**Graphdiyne (GDY) is an artificial carbon allotrope that is conceptually similar to graphene but composed of *sp*- and *sp*$^2$-hybridized carbon atoms. Monolayer GDY (ML-GDY) is predicted to be an ideal 2D semiconductor material with a wide range of applications. However, its synthesis has posed a significant challenge, leading to difficulties in experimentally validating theoretical properties. Here, it is reported that in situ acetylenic homocoupling of hexaethynylbenzene within the sub-nanometer interlayer space of MXene can effectively prevent out-of-plane growth or vertical stacking of the material, resulting in ML-GDY with in-plane periodicity. The subsequent exfoliation process successfully yields free-standing GDY monolayers with micrometer-scale lateral dimensions. The fabrication of field-effect transistor on free-standing ML-GDY makes the first measurement of its electronic properties possible. The measured electrical conductivity ($5.1 \times 10^3$ S m$^{-1}$) and carrier mobility (231.4 cm$^2$ V$^{-1}$ s$^{-1}$) at room temperature are remarkably higher than those of the previously reported multilayer GDY materials. The space-confined synthesis using layered crystals as templates provides a new strategy for preparing 2D materials with precisely controlled layer numbers and long-range structural order.**

## 1. Introduction

Graphdiyne (GDY), composed of periodically arranged *sp*- and *sp*$^2$-hybridized carbon atoms, is an emerging 2D material and a novel carbon allotrope.[1–3] Unlike other carbon allotropes, which typically require harsh synthetic conditions, GDY can be synthesized under mild conditions, such as room temperature and atmospheric pressure. Since the first report of synthetic GDY,[4] substantial efforts have been dedicated to enhancing its quality and controlling its thickness,[5–6] specifically the number of layers.[7–10] Theoretical studies predicted numerous intriguing properties of GDY,[11–16] which can be modulated by tuning the layer number.[17,18] Monolayer GDY (ML-GDY) has attracted particular interest because, unlike zero-bandgap graphene, it exhibits a natural direct bandgap and ultrahigh carrier mobilities.[19–21] ML-GDY's excellent semiconducting properties, combined with its extreme thinness, mechanical robustness,[12,22] and inherent nanoporous structure,[19,23] make it a promising material platform for various applications, including flexible electronics,[9,24] energy storage,[25] and molecular-sieving membranes.[26,27] However, due to the difficulty of preparing GDYs with precisely controlled layer numbers and long-range structural order,[18] the theoretical properties of ML-GDY have not been demonstrated experimentally.

---

J. Li, Q. Liu, C. Chen, G. Li, J. Shen, Z. Lai, Y. Han
Advanced Membranes and Porous Materials Center
Division of Physical Sciences and Engineering
King Abdullah University of Science and Technology
Thuwal 23955-6900, Saudi Arabia
E-mail: jiaqiang.li@kaust.edu.sa; zhiping.lai@kaust.edu.sa

H. Cao, Y. Wu
Division of Computer
Electrical
and Mathematical Science and Engineering
King Abdullah University of Science and Technology
Thuwal 23955-6900, Saudi Arabia

Q. Wang
Imaging and Characterization Core Lab
King Abdullah University of Science and Technology
Thuwal 23955-6900, Saudi Arabia

H. Zhang, Y. Han
Electron Microscopy Center
South China University of Technology
Guangzhou 510640, China

H. Zhang, Y. Han
School of Emergent Soft Matter
South China University of Technology
Guangzhou 510640, China

Z. Shi
State Key Laboratory of Inorganic Synthesis and Preparative Chemistry
College of Chemistry
Jilin University
Changchun 130012, China

The ORCID identification number(s) for the author(s) of this article can be found under https://doi.org/10.1002/adma.202308429

**DOI: 10.1002/adma.202308429**

Acetylenic homocoupling of hexaethynylbenzene (HEB) is the predominant method for GDY synthesis,[18,28] and it has been used to fabricate bulk GDYs with discernible crystallinity.[5,29–30] However, synthesizing ML-GDY remains challenging for two main reasons (Figure S1, Supporting Information). First, the alkyne–aryl and alkyne–alkyne single bonds can freely rotate during the coupling of the HEB monomer, leading to out-of-plane random growth of the framework and eventually to the formation of a 3D disordered structure rather than the desired 2D crystalline structure.[9,31,32] Second, free GDY monolayers tend to stack into multilayers via van der Waals forces and $\pi$–$\pi$ interactions to lower the surface energy.[33,34]

Several synthetic strategies have been developed to overcome these obstacles. Chemical vapor deposition (CVD) was used to grow GDY on an Ag substrate to reduce the degrees of freedom of the HEB monomers. However, only an ill-defined carbonaceous framework was obtained.[35] While recent reports have described the CVD synthesis of ordered multilayer hydrogen-substituted GDY on a single crystal Cu substrate and provided valuable inspirations,[36,37] the successful synthesis of ordered GDY using this method has not yet been demonstrated. Confining the monomer coupling to graphene surfaces,[7,34] oil–water or solid–liquid interfaces,[6,8] and electric double layers [9] yielded GDYs with ordered structures, but in the form of multilayers rather than monolayers. A bulk GDY material was used to prepare ML-GDY by mechanical exfoliation.[10] However, as evidenced by the lack of in-plane X-ray diffraction peaks, the challenge lies in synthesizing pristine bulk GDY crystals with optimal laminar stacking and exceptional purity. Moreover, the physical properties of the obtained ML-GDY, which could in turn provide evidence for the material quality, have never been explored. Therefore, the reliable preparation of crystalline ML-GDY remains a synthetic challenge.

This study reports a confined-space synthesis method that enables the preparation of ML-GDY with in-plane periodicity by using MXene as a template. The primary reason for utilizing MXene as a template is due to its relatively large interlayer spacing and weak interlayer interactions between adjacent $Ti_3C_2T_x$ layers. This characteristic allows various foreign species, including organic molecules and metal ions, to be intercalated without disrupting the crystal structure.[38,39] Consequently, the abundant and regularly spaced interlayer gaps can serve as stable reaction channels for the in-plane coupling of monomer. In this method, HEB monomers diffuse into the periodic interlayer gaps of MXene, where they subsequently polymerize to form the GDY structure in the presence of Cu ions. The sub-nanometer interlayer space of MXene acts as a confinement reactor to effectively suppress the random out-of-plane growth or vertical stacking of GDY. Diffraction, atomic-resolution imaging, and spectroscopic characterizations provide comprehensive and unambiguous evidence for the diffusion, intercalation, and homocoupling of HEB monomers within the MXene interlayer space as well as the formation of ML-GDY therein. The MXene template can be removed by ion intercalation-assisted liquid phase exfoliation to obtain free-standing ML-GDY flakes with micrometer-scale lateral dimensions; this allows the fabrication of field-effect transistor (FET) using ML-GDY for the first time. The ML-GDY device exhibits substantially higher carrier mobility and electrical conductivity than the previously reported multilayer GDY materials.

## 2. Results and Discussion

### 2.1. Growth of ML-GDY in MXene

The preparation of ML-GDY began with selectively etching Al from a dense MAX ($Ti_3AlC_2$) phase using HF to obtain a layer-structured MXene ($Ti_3C_2T_x$; T: OH or F) phase (**Figure 1**a).[38] Note that although MXenes prepared in this way contain mixed OH and F groups at interlayer surfaces,[40,39] the structural models in this report only display OH terminal groups for simplicity.

Scanning electron microscopy (SEM) images revealed that the as-prepared MXene maintained the lateral dimensions (≈10 µm) of the pristine MAX crystals while exhibiting lamellar features along the vertical direction (Figure S2, Supporting Information). Powder X-ray diffraction (PXRD) patterns indicated that the conversion of MAX to MXene resulted in a peak shift of the (002) reflection from 9.53° to 8.82° in $2\theta$, corresponding to an increase in the $d$ spacing from 0.93 to 1.00 nm (Figure 1b).

The as-prepared MXene powders were dispersed in pyridine to expand their interlayer spaces through molecular intercalation, as evidenced by the increase in the $d_{(002)}$ spacing to 1.30 nm (Figure S3, Supporting Information). Next, HEB monomers were introduced into the MXene suspension in pyridine (Figure 1a). The addition of HEB results in a further increase in the $d_{(002)}$ spacing to 1.37 nm (Figure 1b; and Figure S4, Supporting Information), indicating that HEB molecules could also enter the interlayer space of MXene. The Raman spectrum of the resulting material showed a band at 2107 cm$^{-1}$, which is characteristic of the alkyne groups in HEB,[7] confirming the intercalation of HEB into MXene (Figure S5, Supporting Information). Because the limited interlayer space of MXene cannot accommodate "standing" HEB molecules, the intercalated HEB molecules must adopt a horizontal in-plane configuration (Figure S4, Supporting Information). Subsequently, Cu ions were added into the suspension to initiate the Eglinton coupling reaction between HEB monomers (Figure S6, Supporting Information). A portion of the Cu ions diffused into the MXene interlayer space, where they initiated the reaction governed by the steric confinement effect to form ML-GDY. Meanwhile, free Cu ions and HEB monomers in the solution yielded amorphous GDY, which could be largely removed from the GDY-containing MXene by leveraging their markedly different settling velocities in solution (Figures S7 and S8, Supporting Information).

The purified GDY-containing MXene (denoted as GDY-MXene) exhibited the same crystal morphology as the MXene

---

Y. Kong, J. Zhang
Center for Nanochemistry
Beijing Science and Engineering Center for Nanocarbons
Beijing National Laboratory for Molecular Sciences
College of Chemistry and Molecular Engineering
Peking University
Beijing 100871, China
E-mail: jinzhang@pku.edu.cn

Y. Cai, Y. Wu
Division of Physical Sciences and Engineering
King Abdullah University of Science and Technology
Thuwal 23955-6900, Saudi Arabia

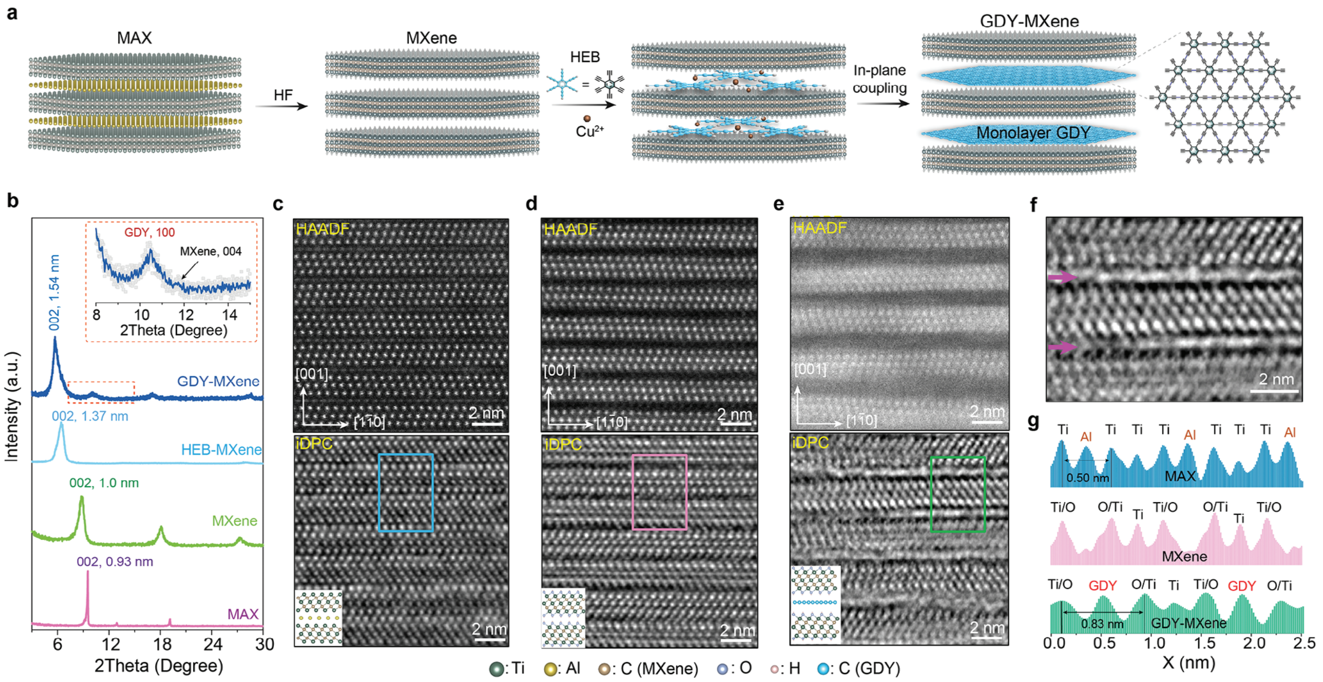

**Figure 1.** Growth of GDY monolayers in MXene. a) Schematic illustration of the process for growing GDY monolayers in the interlayer space of MXene. b) Experimental PXRD patterns of MAX, MXene, HEB-intercalated MXene (HEB-MXene), and GDY-MXene. The inset is a magnified view of the selected region in the PXRD pattern of GDY-MXene, showing the in-plane (100) reflection of GDY. c–e) Atomic-resolution HAADF-STEM (upper panel) and iDPC-STEM (lower panel) images of MAX c), MXene d), and GDY-MXene e) acquired along the [110] zone axis. Insets are the corresponding structural models. f) Magnified iDPC-STEM image of GDY-MXene. Arrows indicate GDY monolayers grown in the interlayer space of MXene. g) Image intensity profiles extracted from the marked areas in (c), (d), and (e). Atomic types of the identified columns are labeled, revealing the distinctly different interlayer structures of the three materials.

template (Figure S9a, Supporting Information). The PXRD result revealed that the in situ growth of GDY resulted in a further increase of the $d_{(002)}$ spacing to 1.54 nm (Figure 1b). This $d$ value corresponds to an available interlayer space of 0.66 nm, which is just enough to accommodate one layer of GDY (Figure S4, Supporting Information). Notably, GDY-MXene exhibited a diffraction peak at $2\theta$ of 10.5° with a $d$ spacing of 0.83 nm, which was larger than the $d_{(004)}$ of MXene while matching the $d_{(100)}$ of the ideal ML-GDY structure (Figure 1b; and Figure S9b, Supporting Information). This result indicates that GDY grown in the MXene interlayer space has in-plane structural order (i.e., is crystalline). Diffraction peaks with higher indexes were not visible because of their weak intensities (Figure S9b, Supporting Information) and the low proportion of ML-GDY compared to MXene.

Control experiments demonstrated that intercalated solvent (i.e., pyridine) molecules could be removed by vacuum heating, as manifested by the restoration of the interlayer spacing of MXene; likewise, intercalated Cu ions could be removed by washing with dilute HCl solution (Figure S10, Supporting Information). In contrast, after the sequential addition of pyridine, HEB, and Cu ions, the significantly expanded interlayer spacing of MXene could not be restored by vacuum heating or HCl washing; this provides additional strong evidence for the formation of an extended GDY framework within MXene.

Scanning transmission electron microscopy (STEM) was used to probe the structural evolution from MAX to MXene and, finally, to GDY-MXene. For each material, high-angle annular dark-field (HAADF) and integrated differential phase-contrast (iDPC)-STEM images were acquired simultaneously to obtain comprehensive structural information; HAADF-STEM can clearly identify the layered structure composed of Ti, whereas iDPC-STEM is more sensitive to the interlayer light elements (Al, O/F, and C).[41] To clearly resolve the atomic columns, the images were all acquired along the [110] zone axis, using specimens prepared with a focused ion beam (Figure S11, Supporting Information).

The HAADF-STEM image of MAX showed alternating $Ti_3$ and Al layers with strong and weak contrast, respectively (Figure 1c). The corresponding iDPC-STEM image showed the Al layers more clearly and even identified the C columns near the Ti columns (Figure 1c; and Figure S12, Supporting Information), due to the enhanced contrast of light elements. The HAADF-STEM image shows that, compared with MAX, MXene has larger but empty spaces between $Ti_3$ layers (Figure 1d). This observation is consistent with the PXRD results and indicates the complete removal of Al by selective etching. The iDPC-STEM image of MXene confirmed the absence of Al layers, while identifying terminal O/F columns on the surfaces of $Ti_3C_2$ layers (Figure 1d; and Figure S13, Supporting Information). Although the HAADF-STEM image of GDY-MXene was blurred by the electron beam-induced carbon contamination, it revealed a significantly expanded interlayer distance (Figure 1e), consistent with the PXRD result. Notably, the iDPC-STEM image clearly showed continuous linear contrast between adjacent $Ti_3C_2T_x$ layers (Figure 1e,f), providing the most direct evidence for the successful growth of ML-GDY within the interlayer space of MXene.

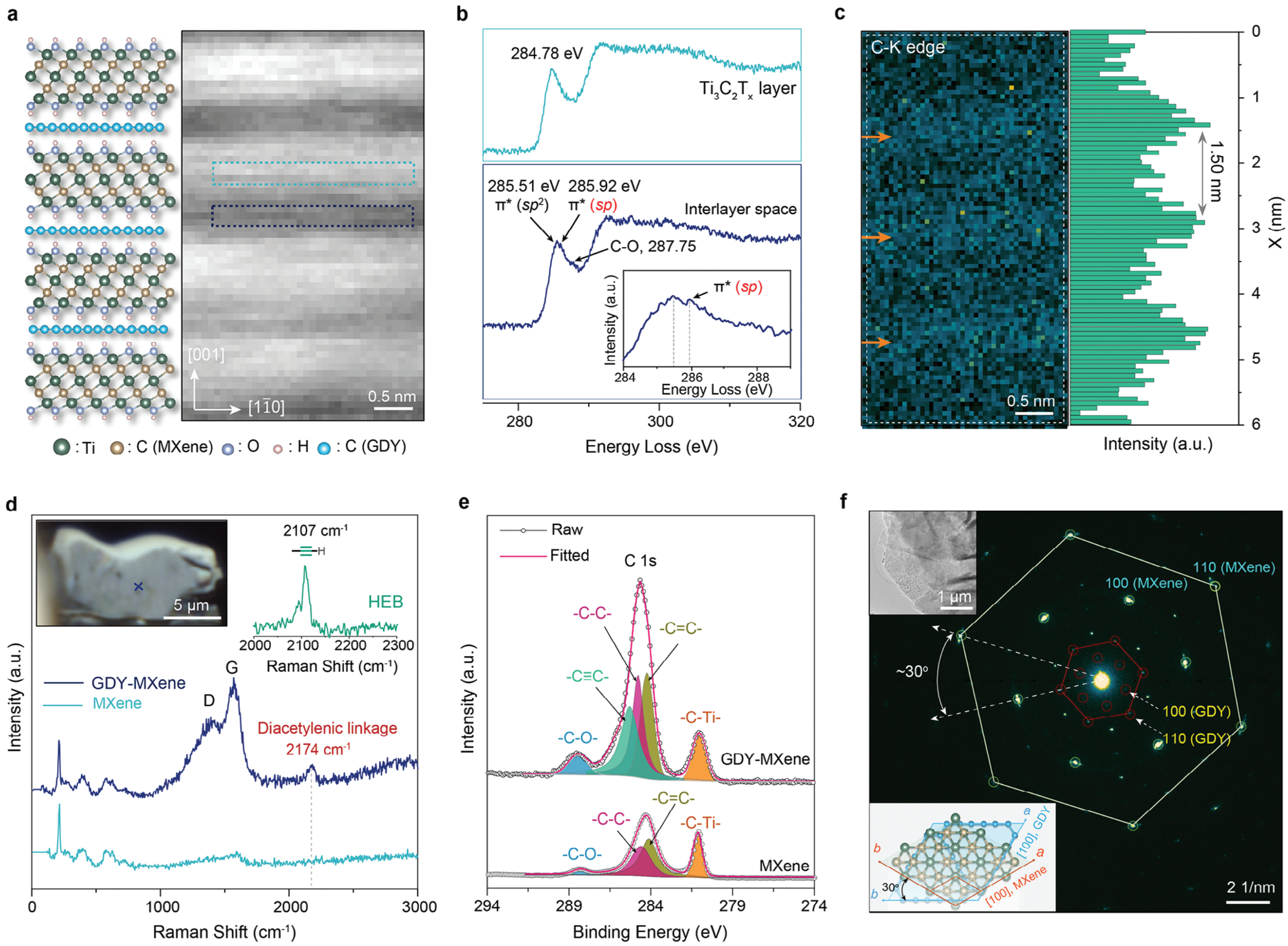

**Figure 2.** Spectroscopic and structural characterization of GDY-MXene. a) Structural model (left) and annular dark field-STEM image (right) of GDY-MXene along the [110] zone axis. b) The C-K edge EELS spectra collected from the $Ti_3C_2T_x$ layer (upper) and interlayer space (lower) in GDY-MXene, as marked in a). The inset shows a magnified view of a portion of the lower spectrum. c) Elemental map (left) and intensity profile (right) based on the C-K edge (285.5–287.5 eV) EELS spectra collected from the region shown in (a), indicating a high carbon content in the interlayer space. d) Raman spectra of MXene and GDY-MXene. The left inset is an optical microscopy image of a GDY-MXene crystal etched using a focused ion beam to expose the internal structure. The cross mark indicates where the Raman spectrum was collected. The right inset shows the Raman spectrum of HEB for comparison. e) High-resolution C1s XPS spectra of MXene and GDY-MXene. f) SAED pattern of GDY-MXene, showing two sets of hexagonal lattices that can be assigned to MXene and GDY structures with a 30° orientation relationship. The upper inset is the TEM image of the GDY-MXene crystal from which the SAED pattern was acquired. The lower inset is a structural model illustrating the orientation relationship between ML-GDY and MXene.

Figure 1g compares the intensity profiles of the marked regions in the iDPC-STEM images, clearly illustrating the differences in the interlayer structure between the three materials. The large-area STEM image of GDY-MXene demonstrates the uniform distribution of ML-GDY throughout the specimen (Figure S14, Supporting Information). Parallel experiments introduce the double amount of HEB also synthesized one-layer GDY between two adjacent $Ti_3C_2T_x$ layers (Figure S15, Supporting Information), demonstrating a self-limiting process in ML-GDY growth within MXene and the reproducibility of this method.

Electron energy loss spectroscopy (EELS) was performed during STEM imaging of GDY-MXene (**Figure 2**a). The high-energy resolution (≈50 meV) allowed probing different chemical states of carbon species. As shown in Figure 2b, the C-K edge EELS spectra acquired from the $Ti_3C_2T_x$ layer and the interlayer space (i.e., ML-GDY) differ in the energy-loss near-edge structure (ELNES). Compared with $Ti_3C_2T_x$,[42] the ELNES of ML-GDY shifts slightly to the high energy region, where the primary peak at 285.51 eV and the shoulder peak at 285.92 eV can be attributed to the 1s→$\pi^*$ excitation of carbon–carbon double bonds and the 1s→$\pi^*$ excitation of carbon–carbon triple bonds, respectively.[43] An additional peak is observed at 287.75 eV, which may originate from the C—O bonds generated by the partial oxidation of ML-GDY.[8] The elemental map based on the C-K edge (285.5–287.5 eV) EELS (Figure 2c) shows stripes with alternating strong and weak intensities, which matches the HAADF-STEM image (Figure 2a) but with the reversed contrast. This result indicates that the carbon content of the interlayer space is higher than that of the $Ti_3C_2T_x$ layer, demonstrating a high filling rate of ML-GDY in MXene.

To avoid possible interference from GDY formed in solution, a focused ion beam was used to remove the outer surface of a

GDY-MXene crystal and then characterized the exposed inner structure using Raman spectroscopy (Figure S16, Supporting Information). The obtained Raman spectrum showed a band at 2174 cm$^{-1}$, which is characteristic of the diacetylenic linkages in the extended network (Figure 2d).[7,9,44,45] During the acquisition of Raman spectra, the laser irradiation would concurrently damage the structure of GDY, leading to the formation of some structural defects, which subsequently results in a large D to G band ratio in the Raman spectra of ML-GDY.[46] The absence of the band associated with terminal alkynes at 2107 cm$^{-1}$ indicates a high degree of HEB coupling, while the appearance of G and D bands provides additional evidence for the formation of GDY within MXene (Figure 2d). Moreover, the Raman intensity map shows a uniform distribution of diacetylenic linkages over the investigated region (Figure S17, Supporting Information). The XPS full spectrum of GDY-MXene after HCl washing indicates that negligible Cu residue is present (Figure S18a, Supporting Information). The spectral fitting results of C 1s XPS show that, compared with MXene, GDY-MXene had an additional peak related to the carbon–carbon triple bond[6,28] and a significantly lower C-Ti peak (Figure 2e; and Figure S18b, Supporting Information). The presence of amorphous carbon with carbon–carbon single and double bonds in MXene has been previously reported and ascribed to contaminants introduced during synthesis.[47] The detection of *sp*-hybridized carbons further evidences the formation of GDY in MXene.

Selected area electron diffraction (SAED) was performed on the periphery of a GDY-MXene crystal, where the crystal was thin enough to allow electron beam penetration. The acquired SAED pattern shows the coexistence of two sets of hexagonal lattices (Figure 2f). The lattice composed of strong diffraction spots with small *d* values can be well indexed based on the [001]-projected MXene structure (a = b = 0.31 nm). The lattice composed of weak diffraction spots with large *d* values matches the SAED pattern simulated from an ideal 2D hexagonal ML-GDY structure (a = b = 0.96 nm) (Figure 2f; and Figure S19, Supporting Information).[6] The SAED result not only reinforces the conclusion from PXRD that the ML-GDY grown in the interlayer space of MXene is crystalline, but also reveals the 30° orientation relationship between ML-GDY and the MXene template (Figure 2f).

### 2.2. Free-Standing GDY Monolayers

MXene can be easily exfoliated into $Ti_3C_2T_x$ monolayers by sonication in solution (Figure S20, Supporting Information),[48] whereas the same treatment cannot decompose GDY-MXene (Figure S21, Supporting Information), implying that the growth of ML-GDY led to stronger interlayer interactions. In order to obtain free-standing GDY monolayers from GDY-MXene (**Figure 3**a), $Li_2SiF_6$ was used to facilitate the liquid-phase exfoliation via $Li^+$ intercalation.[10] The $Li^+$ intercalation into GDY-MXene increased its interlayer spacing (Figure S22, Supporting Information), after which GDY-MXene crystals were decomposed by sonication to form a homogeneous suspension in water (Figure 3b). The powder collected from the suspension was dispersed on a silicon wafer and then characterized using grazing incidence X-ray diffraction. Three reflections were observed, attributed to the (002) and (004) planes of GDY-MXene after $Li^+$ intercalation and the (100) planes of ML-GDY, respectively (Figure S23, Supporting Information). This result demonstrates that the ordered in-plane structure of ML-GDY was preserved during the sonication-assisted exfoliation process, but also indicates that GDY-MXene crystals were not completely exfoliated into GDY and $Ti_3C_2T_x$ monolayers.

Although the obtained powder is a mixture of GDY monolayers, $Ti_3C_2T_x$ monolayers, and residual GDY-MXene sheets, GDY monolayers could be identified by atomic force microscopy (AFM). AFM revealed flakes of different thicknesses, the thinnest region being 0.59 nm (see Figure 3b,c). Given that the thickness of $Ti_3C_2T_x$ monolayer is about 1.5 nm (Figure S24, Supporting Information), flakes with sub-nanometer thicknesses can be assigned to GDY monolayers.[10,35] One potential explanation for the measured thickness being greater than the theoretical thickness of ML-GDY (0.34 nm) could be the entrapment of air or water molecules between the ML-GDY and the $SiO_2/Si$ substrate during the transfer process. Statistics based on AFM observation of 150 GDY monolayers give a lateral dimension distribution of 0.3–2.4 µm centered at 0.75 µm (Figure S25, Supporting Information). Based on the content of ML-GDY gathered from the AFM image statistics and its theoretical density, we estimate its yield to be ≈35.8%. The Raman spectra collected from a sub-nanometer-thick flake (pre-identified using AFM) showed the band characteristics of GDY (Figure 3d). Raman mapping image of diacetylenic linkages (2120–2230 cm$^{-1}$) confirms the homogeneous GDY structure (Figure 3e). The gradually decreasing signal intensity in the Raman spectral series can be attributed to the damaging effect of prolonged laser irradiation (Figure S26, Supporting Information). High-resolution C1s XPS (Figure S27, Supporting Information) of the sub-nanometer flake is composed of *sp*- and *sp*$^2$-hybridized carbon which is consistent with the structure of GDY.

Under transmission electron microscopy (TEM), free-standing GDY monolayers can be identified from the weakest image contrast combined with the lack of Ti element determined by EELS or energy-dispersive X-ray spectroscopy (Figure S28, Supporting Information). The acquired SAED pattern well matches with simulated SAED pattern of ML-GDY (Figure 3f; and Figure S18, Supporting Information), indicating the in-plane periodicity of ML-GDY is retained after exfoliating from MXene interlayer. It was found that the diffraction spots rapidly disappeared during SAED, suggesting that the structure of ML-GDY is extremely sensitive to electron beam irradiation. Moreover, free-standing ML-GDY continuously vibrates and drifts under the electron beam. Therefore, it is challenging to obtain a high-resolution TEM (HRTEM) image that showcases the inherent structure. The HRTEM image we were able to capture, combined with its fast Fourier transformation (FFT), further reveals the periodicity of free-standing GDY monolayers (Figure S29, Supporting Information). We compared the EELS spectra collected from a free-standing ML-GDY and the amorphous carbon film of the TEM grid (Figure 3g,h). In the low-loss region, the spectrum of ML-GDY reveals a bandgap of 1.04 eV, which is in good agreement with the theoretical prediction using the first-principles calculations;[49] in contrast, the spectrum of amorphous carbon film showed no bandgap excitation (Figure 3g). In the core-loss

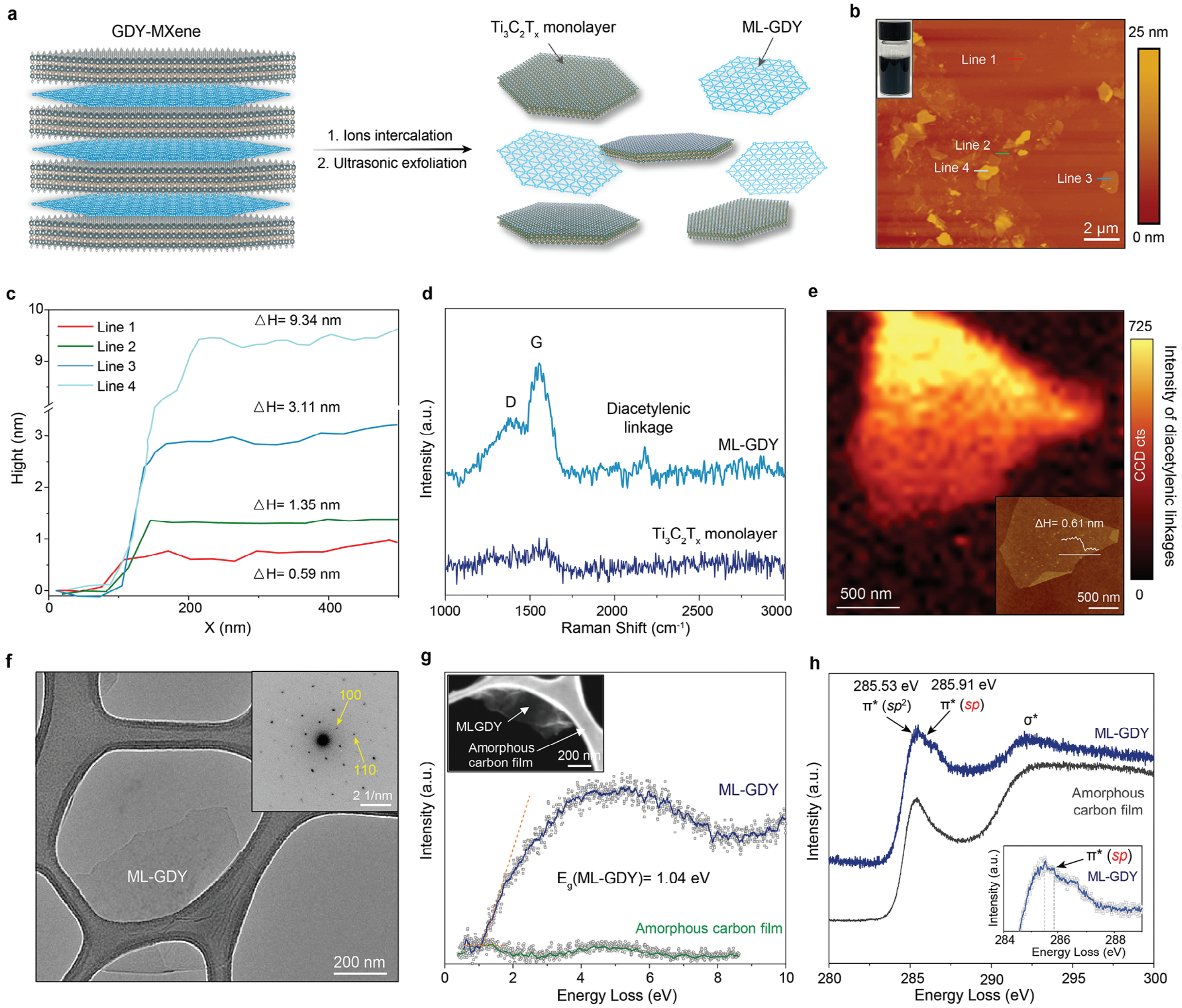

**Figure 3.** Preparation and characterization of free-standing ML-GDY. a) Schematic illustration showing the preparation of free-standing ML-GDY from GDY-MXene by ion intercalation-assisted exfoliation. b) AFM image of the exfoliated GDY-MXene powder, showing a mixture of flakes of different thicknesses. Inset is a photograph of the suspension obtained after the exfoliation process. c) AFM height profiles of the four labeled flakes in (b). d) Raman spectra of a ML-GDY and $Ti_3C_2T_x$ monolayer flakes (preidentified using AFM). e) Raman intensity map of a ML-GDY flake based on the signals at 2120–2230 cm$^{-1}$. Inset is the corresponding AFM image. The indicated height of 0.61 nm corresponds to the lowest value in the profile. f) TEM images of a free-standing ML-GDY and SAED pattern (inset). Low-loss g) and core-loss h) EELS spectra collected from free-standing ML-GDY and the amorphous carbon film of the TEM grid. Inset in (g) is a STEM image of the area where the EELS was conducted. Inset in (h) is the magnified EELS spectrum of ML-GDY.

region, ML-GDY exhibits a shoulder peak at 285.91 eV, associated with the 1s→$\pi^*$ excitation of *sp* carbon bonded carbon–carbon triple bonds,[43] which is not observed in the spectrum of amorphous carbon (Figure 3h). Moreover, the amorphous carbon has stronger $\sigma^*$ excitation than ML-GDY, suggesting a higher density of $sp^3$ carbon (Figure 3h). These results demonstrate that, despite the inevitable partial structural damage during EELS, free-standing ML-GDY displays distinctly different properties from amorphous carbon, including a well-defined bandgap and the presence of *sp*-hybridized carbon.

### 2.3. Electronic Properties of ML-GDY

Semiconducting 2D materials are considered critical for the development of next-generation electronic devices. Theoretical studies indicate that GDY is a semiconductor with electronic properties varying with the number of layers. To date, only multilayer GDY materials have been tested.[4,7,8,21,34,50–53] The confined-space synthesis reported here enables the preparation of isolated ML-GDY, thus allowing the first measurement of its electronic properties by fabricating a series of FET devices.

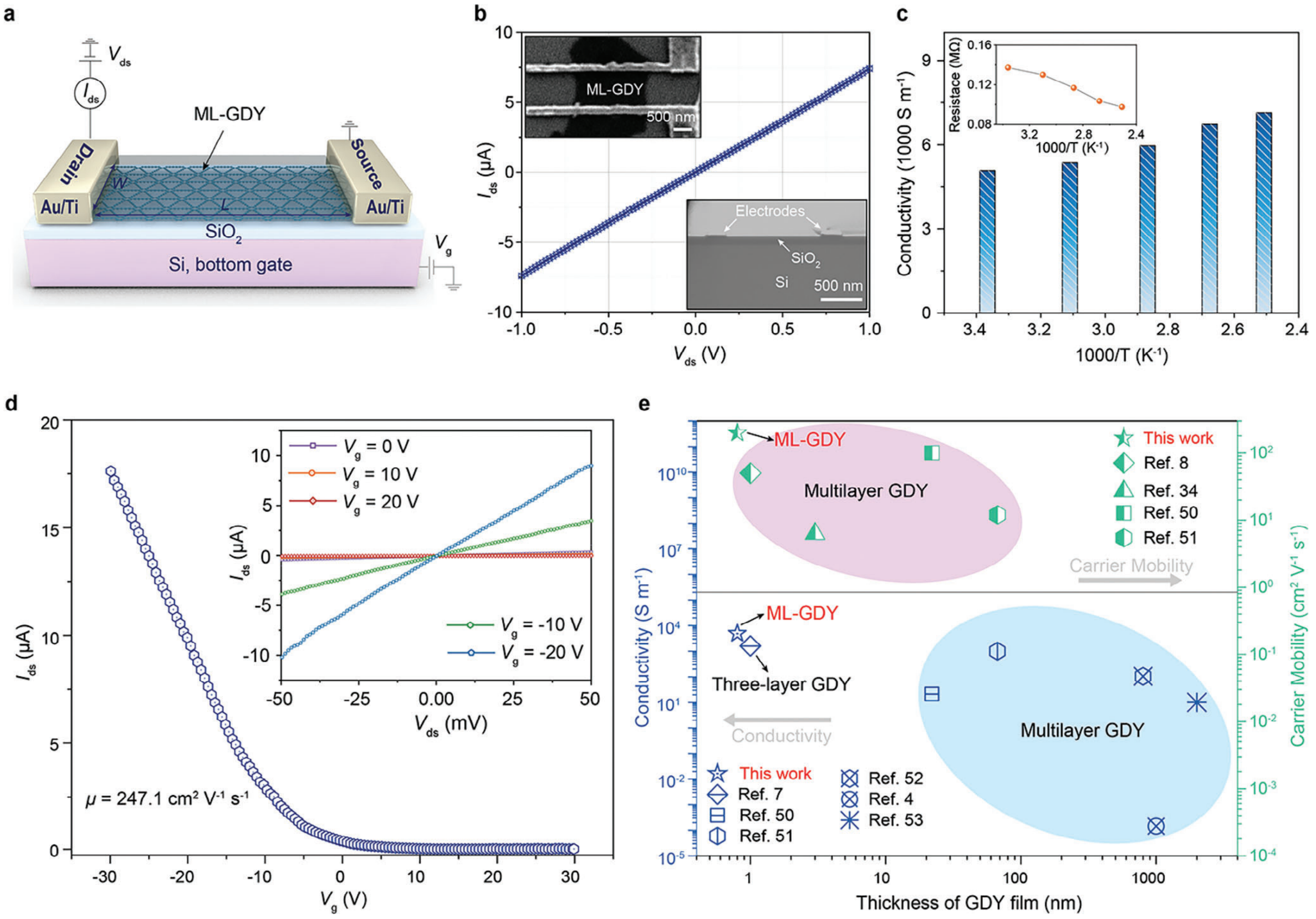

**Figure 4.** Fabrication and measurements of ML-GDY FETs. a) Schematic illustration of the structure of the ML-GDY FET device. b) $I_{ds}-V_{ds}$ characteristic of ML-GDY measured at 298 K. The upper left inset is a top-view SEM image of the device and bottom right is a cross-sectional HAADF-STEM image of the device. c) Conductivities and resistances (inset) of ML-GDY as an inverse function of temperature. d) Transfer characteristic curve of the ML-GDY FET at $V_{ds} = 0.05$ V. The inset shows output characteristic curves of ML-GDY FET recorded under various $V_g$ biases from −20 to 20 V. e) Comparisons of ML-GDY with previously reported multilayer GDY materials in conductivity and carrier mobility.

The ML-GDY FET was fabricated by depositing Au/Ti on ML-GDY as source and drain terminals and using single-crystal Si as the bottom gate and $SiO_2$ as the dielectric layer (**Figure 4**a; and Figure S30, Supporting Information). The AFM and Raman characterization results confirmed that the devices were fabricated on ML-GDY (Figure S31, Supporting Information). The gate leakage current density of the fabricated ML-GDY FET was as low as $10^{-3}$ A cm$^{-2}$ at ± 30 V (Figure S32a, Supporting Information), confirming the excellent insulating properties of the dielectric $SiO_2$ layer. The linear $I_{ds}$–$V_{ds}$ curve measured at 298 K indicated an ohmic contact between ML-GDY and electrodes (Figure 4b), and the calculated conductivity of ML-GDY was $5.1 \times 10^3$ S m$^{-1}$. The conductivity of ML-GDY increased with the measurement temperature and reached $7.1 \times 10^3$ S m$^{-1}$ at 398 K (Figure 4c; and Figure S32b, Supporting Information). This behavior suggests that ML-GDY is a semiconductor while demonstrating its good thermal stability.

The transfer characteristic curve (at $V_{ds} = 0.05$ V) of the ML-GDY FET showed a spurt in current growth at $V_g = \approx 2.5$ V. The current reduction during the forward sweep of $V_g$ indicated hole-dominated conduction and thus the *p*-type nature of ML-GDY (Figure 4d).[8,34] The output characteristic curves of the device exhibited an obvious evident gate control property (Figure 4d, inset), which was not observed in previously reported multilayer GDY-based FETs. The carrier mobility of ML-GDY was calculated using the equation $\mu = [dI_{ds}/dV_g][L/(WC_g V_{ds})]$,[54] where $L$ is the channel length of the FET, $W$ is the width of ML-GDY (see Figure 4a), and $C_g = 34.5$ nF cm$^{-2}$. The calculated carrier mobilities from three independent FET devices were 247.1, 213.7, and 233.3 cm$^2$ V$^{-1}$ s$^{-1}$ (Figure S33 and Table S1, Supporting Information), respectively, with an average value of 231.4 cm$^2$ V$^{-1}$ s$^{-1}$. Furthermore, the ML-GDY-based device showcases a notable $I_{on}/I_{off}$ ratio of $1.2 \times 10^3$, indicating its potential applications of FETs.

As summarized in Figure 4e, ML-GDY exhibits higher electrical conductivity and carrier mobility than previous multilayer GDY materials prepared using various methods (see details in Table S2, Supporting Information). ML-GDY also shows comparable electronic properties with other 2D materials synthesized through solution methods (Table S3, Supporting Information). ML-GDY's outstanding electronic properties can be attributed to its high structural order achieved by the confined-space synthesis and single-atom thickness. Nevertheless, the measured carrier mobility of ML-GDY is still considerably lower than theoretical prediction values, which may be due to the partial structural damage of ML-GDY and the introduction of contamination during the fabrication of the FET devices.

## 3. Conclusion

High-quality materials with well-defined structures provide the basis for reliable mechanistic and performance studies. Despite numerous research efforts, the synthesis of crystalline monolayer GDY remains a grand challenge, hindering the development of its applications. In this work, we demonstrated that the limited interlayer space in MXene can be exploited to facilitate the 2D growth of GDY and avoid vertical stacking. The efficient generation of ordered GDY monolayers throughout MXene crystals was fully demonstrated by combined diffraction, atomic-resolution imaging, and spectroscopic characterization. Free-standing ML-GDY flakes with micrometer-scale lateral dimensions were obtained from the GDY-MXene composite via ion intercalation-assisted liquid-phase exfoliation, and their retained in-plane periodicity and single-atom thickness were verified. Free-standing ML-GDY allows the fabrication of unprecedented ML-GDY FETs. According to FET measurements, the as-prepared ML-GDY behaves as a *p*-type semiconductor, exhibiting an average carrier mobility of 231.4 $\text{cm}^2\ \text{V}^{-1}\ \text{s}^{-1}$ and a conductivity of $5.1 \times 10^3$ S $\text{m}^{-1}$ at room temperature, which is superior to various previously reported multilayer GDY materials. The synthetic strategy developed in this work represents a new route to fabricating monolayer 2D structures not viable using conventional synthesis.

## 4. Experimental Section

*Preparation of MXene*: The MXene material was prepared from a commercial MAX ($Ti_3AlC_2$) phase using an established method.[38] In a typical procedure, 1 g of MAX was added to an argon-filled Teflon reactor, followed by 20 mL of HF solution (30%) under stirring, and continued at room temperature for 22 h. The sediment was collected by centrifugation (10 min, 8000 rpm) and washed by deionized $H_2O$ repeatedly until the pH of the supernatant reached neutral. The obtained powder (MXene) was freeze-dried.

*Synthesis of HEB*: Tetrabutylammonium fluoride (1 м in THF, 0.5 mL) was added to 20 mL of THF containing 50 mg of hexakis[(trimethylsilyl)-ethynyl]benzene under an argon atmosphere, and the mixture was stirred at 0 °C for 15 min. The mixture was then washed twice with 50 mL of saturated NaCl solution, dried over anhydrous $MgSO_4$, and filtered. The solvent was evaporated, and the residue was redissolved in 20 mL of EtOAc. The solution was purified by chromatography using a short silica gel column (length: 2 cm; diameter: 2.5 cm). Finally, the solvent was removed by evaporation, and the obtained white solid (HEB) was dissolved in 5 mL of EtOAc. Note that since HEB is unstable at room temperature and sensitive to oxygen, all these procedures should be performed quickly in the dark and the HEB solution should be stored at 4 °C under argon. The $^1$H NMR (400 MHz, DMSO) and $^{13}$C NMR (125 MHz, DMSO) spectra of HEB are presented in Figure S34 (Supporting Information).

*Growth of ML-GDY in MXene*: MXene powder (50 mg) was dispersed in 20 mL of pyridine under an argon atmosphere, and the obtained suspension was ultrasonicated for 5 min. Then, 5 mL of HEB solution prepared in the previous step was dropwise added into the MXene suspension, and the resulting mixture was stirred at 0 °C for 5 h. Next, 5 mL of pyridine containing 25 mg of $Cu(OAc)_2$ was added. After 24 h of reaction at room temperature under static conditions, the supernatant was carefully removed and the solid was collected by filtration and washed by pyridine, *N,N*-dimethylformamide, and water successively. To remove residual Cu, the solid was immersed in 10 mL of 0.5 м HCl for 10 h. Finally, the solid was collected by filtration, washed thoroughly with deionized water and ethanol, and air dried.

The resultant powder was subjected to a separation process to remove amorphous GDY formed in solution from GDY-MXene crystals by leveraging their different settling velocity. In brief, 50 mg of the powder was dispersed in 20 mL of deionized water and stirred for 10 min to obtain a suspension. This suspension was then allowed to settle undisturbed for 15 min. Subsequently, the upper aqueous dispersion was gently removed and the settled precipitate was gathered through filtration. This process was repeated thrice. Finally, the purified GDY-MXene was left to air dry.

*Preparation of Free-Standing ML-GDY*: Free-standing GDY monolayers were prepared using ion intercalation-assisted liquid phase exfoliation. Typically, 50 mg of $Li_2SiF_6$ was added to 20 mL of water, followed by 20 mg of GDY-MXene. The mixture was continuously stirred at 25 °C for 48 h under an inter gas atmosphere to ensure complete intercalation of Li into GDY-MXene. The Li-intercalated GDY-MXene was collected by centrifugation (8000 rpm for 15 min) and washed thoroughly with deionized water to remove the residual $Li_2SiF_6$. The obtained solid was dispersed in 50 mL of $H_2O$ and then ultrasonicated (power: 1000 W) at 0 °C for 30 min. The resulting homogenous suspension contained GDY monolayers, $Ti_3C_2T_x$ monolayers, and incompletely exfoliated GDY-MXene sheets.

*Fabrication and Measurements of ML-GDY FETs*: A 1 × 1 cm $SiO_2$ (100 nm)/Si (0.5 mm) substrate was treated with $O_2$ plasma for 10 s. Then, 10 µL of the suspension containing GDY monolayers (i.e., the suspension that had undergone the exfoliation process) was added dropwise on the $SiO_2$/Si substrate. After air drying, the substrate was kept under vacuum at 60 °C for 2 h. Then, electrode patterns were fabricated on ML-GDY flakes using electron beam lithography. Gold and titanium stacks with thicknesses of 100 and 10 nm, respectively, were deposited as electrodes by sputter coating and lift-off procedures to form a ML-GDY FET with a 1 µm channel length. A semiconductor analyzer (Keithley 4200SCS) was used to determine the conductivity and transfer characteristics of the ML-GDY FET. The *I–V* curves at different temperatures were measured using a Keithley 4200SCS with a heating stage (IKA RCT 5 digital).

The calculation of mobility is based on the following equations

$$\mu = \left[\frac{dI_{ds}}{dV_g}\right]\left[\frac{L}{WC_gV_{ds}}\right] \tag{1}$$

$$C_g = \frac{\varepsilon_r\varepsilon_0}{d} \tag{2}$$

where $L$ is the channel length of the FET, $W$ is the width of the ML-GDY flake, $d$ is the thickness of the $SiO_2$ layer, $\epsilon_r$ is the dielectric constant of $SiO_2$, and $\epsilon_0$ is the vacuum dielectric constant.

The calculation of conductivity is based on the following equation

$$\delta = \frac{L}{RWH} \tag{3}$$

where $L$ and $R$ are the channel length and resistance of the ML-GDY FET, respectively; $W$ and $H$ are the width and thickness of ML-GDY, respectively.

## Supporting Information

Supporting Information is available from the Wiley Online Library or from the author.

## Acknowledgements

J.L. and H.C. contributed equally to this work. The authors thanked Xiangming Xu and Xuanzhang Li for providing suggestions on device fabrication. Financial support for this work was provided by King Abdullah University of Science and Technology (KAUST) Baseline Funds (Nos. BAS/1/1372-01-01 and BAS/1/1375-01-01) to Y.H. and Z.L., Ministry of Science and Technology of China (Nos. 2018YFA0703502 and 2016YFA0200100) to J.Z., and KAUST Competitive Research Grant (No. OSR-CRG2020-4374) to Y.W..

## Conflict of Interest

The authors declare no conflict of interest.

## Data Availability Statement

The data that support the findings of this study are available in the supplementary material of this article.

## Keywords

confined-space, electronic properties, graphdiyne, monolayer, MXene interlayer

Received: August 19, 2023
Revised: October 10, 2023

---

[1] C. Huang, Y. Li, N. Wang, Y. Xue, Z. Zuo, H. Liu, Y. Li, *Chem. Rev.* **2018**, *118*, 7744.
[2] A. Hirsch, *Nat. Mater.* **2010**, *9*, 868.
[3] Z. Jia, Y. Li, Z. Zuo, H. Liu, C. Huang, Y. Li, *Acc. Chem. Res.* **2017**, *50*, 2470.
[4] G. Li, Y. Li, H. Liu, Y. Guo, Y. Li, D. Zhu, *Chem. Commun.* **2010**, *46*, 3256.
[5] C. Zhang, Y. Xue, X. Zheng, L. Qi, Y. Li, *Mater. Today* **2023**, *66*, 72.
[6] R. Matsuoka, R. Sakamoto, K. Hoshiko, S. Sasaki, H. Masunaga, K. Nagashio, H. Nishihara, *J. Am. Chem. Soc.* **2017**, *139*, 3145.
[7] X. Gao, Y. Zhu, D. Yi, J. Zhou, S. Zhang, C. Yin, F. Ding, S. Zhang, X. Yi, J. Wang, L. Tong, Y. Han, Z. Liu, J. Zhang, *Sci. Adv.* **2018**, *4*, eaat6378.
[8] C. Yin, J. Li, T. Li, Y. Yu, Y. Kong, P. Gao, H. Peng, L. Tong, J. Zhang, *Adv. Funct. Mater.* **2020**, *30*, 2001396.
[9] J. Li, Z. Zhang, Y. Kong, B. Yao, C. Yin, L. Tong, X. Chen, T. Lu, J. Zhang, *Chem* **2021**, *7*, 1284.
[10] H. Yan, P. Yu, G. Han, Q. Zhang, L. Gu, Y. Yi, H. Liu, Y. Li, L. Mao, *Angew. Chem., Int. Ed.* **2019**, *58*, 746.
[11] L. D. Pan, L. Z. Zhang, B. Q. Song, S. X. Du, H.-J. Gao, *Appl. Phys. Lett.* **2011**, *98*, 173102.
[12] Y. Yang, X. Xu, *Comput. Mater. Sci.* **2012**, *61*, 83.
[13] H.-J. Cui, X.-L. Sheng, Q.-B. Yan, Q.-R. Zheng, G. Su, *Phys. Chem. Chem. Phys.* **2013**, *15*, 8179.
[14] A. L. Ivanovskii, *Prog. Solid State Chem.* **2013**, *41*, 1.
[15] S. Jalili, F. Houshmand, J. Schofield, *Appl. Phys. A* **2015**, *119*, 571.
[16] Y. Zheng, Y. Chen, L. Lin, Y. Sun, H. Liu, Y. Li, Y. Du, N. Tang, *Appl. Phys. Lett.* **2017**, *111*, 033101.
[17] Q. Zheng, G. Luo, Q. Liu, R. Quhe, J. Zheng, K. Tang, Z. Gao, S. Nagase, J. Lu, *Nanoscale* **2012**, *4*, 3990.
[18] Y. Kong, J. Li, S. Zeng, C. Yin, L. Tong, J. Zhang, *Chem* **2020**, *6*, 1933.
[19] Y. Li, L. Xu, H. Liu, Y. Li, *Chem. Soc. Rev.* **2014**, *43*, 2572.
[20] M. Long, L. Tang, D. Wang, Y. Li, Z. Shuai, *ACS Nano* **2011**, *5*, 2593.
[21] J. Chen, J. Xi, D. Wang, Z. Shuai, *J. Phys. Chem. Lett.* **2013**, *4*, 1443.
[22] S. Pari, A. Cuéllar, B. M. Wong, *J. Phys. Chem. C* **2016**, *120*, 18871.
[23] M. M. Haley, S. C. Brand, J. J. Pak, *Angew. Chem., Int. Ed.* **1997**, *36*, 836.
[24] Y. Zhang, P. Huang, J. Guo, R. Shi, W. Huang, Z. Shi, L. Wu, F. Zhang, L. Gao, C. Li, X. Zhang, J. Xu, H. Zhang, *Adv. Mater.* **2020**, *32*, 2001082.
[25] N. Wang, J. He, K. Wang, Y. Zhao, T. Jiu, C. Huang, Y. Li, *Adv. Mater.* **2019**, *31*, 1803202.
[26] M. Bartolomei, E. Carmona-Novillo, M. I. Hernández, J. Campos-Martínez, F. Pirani, G. Giorgi, K. Yamashita, *J. Phys. Chem. Lett.* **2014**, *5*, 751.
[27] L. Fang, Z. Cao, *J. Phys. Chem. C* **2020**, *124*, 2712.
[28] J. Zhou, X. Gao, R. Liu, Z. Xie, J. Yang, S. Zhang, G. Zhang, H. Liu, Y. Li, J. Zhang, Z. Liu, *J. Am. Chem. Soc.* **2015**, *137*, 7596.
[29] C. Li, X. Lu, Y. Han, S. Tang, Y. Ding, R. Liu, H. Bao, Y. Li, J. Luo, T. Lu, *Nano Res.* **2018**, *11*, 1714.
[30] X. Luan, L. Qi, Z. Zheng, Y. Gao, Y. Xue, Y. Li, *Angew. Chem., Int. Ed.* **2023**, *62*, e202215968.
[31] J. Sakamoto, J. Van Heijst, O. Lukin, A. D. Schlüter, *Angew. Chem., Int. Ed.* **2009**, *48*, 1030.
[32] J. Zhou, J. Li, Z. Liu, J. Zhang, *Adv. Mater.* **2019**, *31*, 1803758.
[33] J. W. Colson, A. R. Woll, A. Mukherjee, M. P. Levendorf, E. L. Spitler, V. B. Shields, M. G. Spencer, J. Park, W. R. Dichtel, *Science* **2011**, *332*, 228.
[34] J. Zhou, Z. Xie, R. Liu, X. Gao, J. Li, Y. Xiong, L. Tong, J. Zhang, Z. Liu, *ACS Appl. Mater. Interfaces* **2018**, *11*, 2632.
[35] R. Liu, X. Gao, J. Zhou, H. Xu, Z. Li, S. Zhang, Z. Xie, J. Zhang, Z. Liu, *Adv. Mater.* **2017**, *29*, 1604665.
[36] J. Shen, Y. Cai, C. Zhang, W. Wei, C. Chen, L. Liu, K. Yang, Y. Ma, Y. Wang, C.-C. Tseng, J.-H. Fu, X. Dong, J. Li, X.-X. Zhang, L.-J. Li, J. Jiang, I. Pinnau, V. Tung, Y. Han, *Nat. Mater.* **2022**, *21*, 1183.
[37] Y. Cai, J. Shen, J.-H. Fu, N. Qaiser, C. Chen, C.-C. Tseng, M. Hakami, Z. Yang, H.-J. Yen, X. Dong, L.-J. Li, Y. Han, V. Tung, *ACS Nano* **2022**, *16*, 16677.
[38] M. R. Lukatskaya, O. Mashtalir, C. E. Ren, Y. Dall'agnese, P. Rozier, P. L. Taberna, M. Naguib, P. Simon, M. W. Barsoum, Y. Gogotsi, *Science* **2013**, *341*, 1502.
[39] O. Mashtalir, M. Naguib, V. N. Mochalin, Y. Dall'agnese, M. Heon, M. W. Barsoum, Y. Gogotsi, *Nat. Commun.* **2013**, *4*, 1716.
[40] M. Naguib, M. Kurtoglu, V. Presser, J. Lu, J. Niu, M. Heon, L. Hultman, Y. Gogotsi, M. W. Barsoum, *Adv. Mater.* **2011**, *23*, 4248.
[41] E. Yücelen, I. Lazic, E. G. T. Bosch, *Sci. Rep.* **2018**, *8*, 2676.
[42] D. Magne, V. Mauchamp, S. Célérier, P. Chartier, T. Cabioc'h, *Phys. Chem. Chem. Phys.* **2016**, *18*, 30946.
[43] J. Zhong, J. Wang, J.-G. Zhou, B.-H. Mao, C.-H. Liu, H.-B. Liu, Y.-L. Li, T.-K. Sham, X.-H. Sun, S.-D. Wang, *J. Phys. Chem. C* **2013**, *117*, 5931.
[44] S. Zhang, J. Wang, Z. Li, R. Zhao, L. Tong, Z. Liu, J. Zhang, Z. Liu, *J. Phys. Chem. C* **2016**, *120*, 10605.
[45] Y. Dong, S. Semin, Y. Feng, J. Xu, T. Rasing, *Chin. Chem. Lett.* **2021**, *32*, 525.
[46] Y. Zhang, R. Shi, A. Kuklin, C. Ma, H. Chen, Y. Shu, X. Liu, Y. Fu, B. O. Al-Amoudi, S. Wageh, A. A. Al-Ghamdi, H. Ågren, J. Xu, H. Zhang, *Nano Today* **2022**, *47*, 101653.
[47] V. Natu, M. Benchakar, C. Canaff, A. Habrioux, S. Célérier, M. W. Barsoum, *Matter* **2021**, *4*, 1224.
[48] J. Zhang, N. Kong, S. Uzun, A. Levitt, S. Seyedin, P. A. Lynch, S. Qin, M. Han, W. Yang, J. Liu, X. Wang, Y. Gogotsi, J. M. Razal, *Adv. Mater.* **2020**, *32*, 2001093.
[49] G. Luo, X. Qian, H. Liu, Q. Rui, Z. Jing, L. Li, Z. Gao, E. Wang, W. N. Mei, L. Jing, *Phys. Rev. B* **2011**, *84*, 2250.
[50] X. Qian, H. Liu, C. Huang, S. Chen, L. Zhang, Y. Li, J. Wang, Y. Li, *Sci. Rep.* **2015**, *5*, 7756.

[51] Y. Li, M. J. Zhang, X. L. Hu, X. H. Fan, L. M. Yu, C. S. Huang, *J. Phys. Chem. Lett.* **2020**, *11*, 1998.

[52] F. Zhao, N. Wang, M. Zhang, A. Sápi, J. Yu, X. Li, W. Cui, Z. Yang, C. Huang, *Chem. Commun.* **2018**, *54*, 6004.

[53] Z. Zuo, H. Shang, Y. Chen, J. Li, H. Liu, Y. Li, Y. Li, *Chem. Commun.* **2017**, *53*, 8074.

[54] B. Radisavljevic, A. Radenovic, J. Brivio, V. Giacometti, A. Kis, *Nat. Nanotechnol.* **2011**, *6*, 147.